What Cause the Common-Mode Error in Array GPS Displacement Fields: Case Study for Taiwan in Relation to Atmospheric Mass Loading

Utpal Kumar[1,2,3], Benjamin Fong Chao[1*], and Emmy T. Y. Chang[4]

[1]Institute of Earth Sciences, Academia Sinica, Taipei, Taiwan.

[2]Taiwan International Graduate Program (TIGP), Academia Sinica, Taipei, Taiwan.

[3]College of Earth Sciences, National Central University, Zhongli, Taiwan.

[4]Institute of Oceanography, National Taiwan University, Taipei, Taiwan.

Corresponding author: Benjamin Fong Chao (bfchao@earth.sinica.edu.tw)

Key Points:

- Taiwan's dense GPS network data show strong spatially coherent vertical displacement and seasonality.
- Common-mode errors (CME) solved using empirical orthogonal functions correlates well with the atmospheric mass loading.
- Up to 90% of CME can be quantitatively attributed to the non-seasonal atmospheric mass loading displacements.

Abstract

We analyze forty-seven best-quality, ten-year-long daily Global Positioning System (GPS) position time series of Taiwan, to understand the origin of the GPS's common-mode error (CME) whose seasonality in the standard deviation evidences a meteorological origin. We employ the efficient Empirical Orthogonal Function analysis to extract the CME as the leading island-wide mode for all three components (whereas the second mode relates to the El Niño-Southern Oscillation). We find that the CME correlates well with the acquired variations in the atmospheric mass loading (AML) displacement field for Taiwan courtesy of NASA Goddard Space Flight Center for the vertical component with high coherence around 11-14 cycles per year. Further regression analysis shows that up to 90% of the non-seasonal AML displacements in Taiwan are evident in the CME variations.

Plain Language Summary

The extracted common-mode error - long period, high amplitude, in-phase daily fluctuations, from the continuous GPS data, is compared with the atmospheric mass loading displacements in Taiwan. The time and frequency domain correlation study shows a significant correlation between the two in between 26-33 days/cycle with lag around or less than one day. Up to 90% of the common-mode error variations can be explained by the quantitative variations in atmospheric mass loading.

1 Introduction

Continuous Global Positioning System (GPS) observations provide an efficient measurement of the time-dependent displacement field for the understanding of processes of the Earth's crust such as fault motion detection (Heki et al., 2006; Malet et al., 2002; Massonnet et al., 1996; Wdowinski et al., 2004), postglacial rebound (Johansson et al., 2002), postseismic deformation (Dragert et al., 2001; Hudnut et al., 2002; Miller et al., 2002), and seasonal and transient changes (Bock et al., 2004; Dong, Fang, Bock, Cheng, & Miyazaki, 2002a; Hatanaka et al., 2014; Larson et al., 2003; Melbourne & Webb, 2002; vanDam et al., 1994). In practice any systematic errors in the GPS end-products, if not treated properly, may contaminate or bias the geophysical interpretations and applications. In regional networks especially in the tropical and subtropical regions, a dominant systematic error exhibits strong spatial coherence, with amplitudes as high as a few centimeters on the timescales of a few days to several months. It is commonly known as the common-mode errors (CME), or common-mode signals depending on the context. It is thought to be the aggregative outcome of errors in the preprocessing techniques, alignment to reference frame, modeling of satellites (orbits, clocks, antenna phase center), modeling of tropospheric and ionospheric media, and geophysical phenomena such as thermal expansion, large-scale atmospheric and hydrological effects (Dong et al., 2006; Gruszczynski et al., 2019; King et al., 2010; Wdowinski et al., 1997; Zhu, Zhou, Deng, et al., 2017).

Several filtering techniques have been developed to extract the CME from the GPS data based on the assumption of CME being spatially and temporally correlated (Blewitt & Lavallee, 2002; Gruszczynski et al., 2019; Miyazaki et al., 2003; Smith et al., 2004; Teferle et al., 2006;

Wdowinski et al., 1997; Williams et al., 2004). CME is traditionally extracted by applying the regional spatial processing (Ching et al., 2007; Wdowinski et al., 1997; Zhang et al., 2016; Zhu, Zhou, & Liu, 2017), for example, by estimating the mean of the stack of position residuals. This method has limitations when extended over extensive networks (maximum inter-station distance of 600 km) where the assumption of spatial uniformity breaks down (Gruszczynski et al., 2019; Márquez-Azúa & DeMets, 2003; Wdowinski et al., 1997; Williams et al., 2004). The CME can also be reduced via a similarity transformation algorithm (Blewitt et al., 2013). Alternatively, *Dong et al*. (2006) proposed the spatio-temporal filtering of GPS data using the combination of Principal Component Analysis (PCA) and the Karhunen-Loeve expansion. Empirical Orthogonal Function (EOF) decomposition, a form of PCA, provides a more robust numerical framework for the segregation of the signal and the CME from the regional GPS records than the stacking approach (Dong et al., 2006; Gruszczynski, 2016; Serpelloni et al., 2013), by allowing for the non-uniform spatial response of the network stations to a CME source and also accounting for the timespans and the inter-station distances hence less sensitive to the abnormal single station data (Márquez-Azúa & DeMets, 2003; Tian & Shen, 2016).

Detection of small scale crustal deformations in the GPS time series as a result of the atmospheric mass loading effects has been acknowledged in multiple studies (e.g. Dong, Fang, Bock, Cheng, & Miyazaki, 2002b; Tregoning & van Dam, 2005; vanDam & Herring, 1994). Some studies (Dong et al., 2006; Yuan et al., 2008) found these crustal deformations to contribute to the spatially correlated “errors” in the GPS data. Recent studies (Gruszczynska et al., 2019; Gruszczynski et al., 2019; Zhu, Zhou, & Liu, 2017) have further explored the relation of CME with the environmental sources. Zhu et al. (2017) examined the effects of environmental loading and thermal expansion on the estimated CME from large network of the Crustal Movement Observation Network of China. They found that the environmental loading corrections on the CME reduces the inter-station correlation coefficients of the vertical component up to 20% and that the thermal expansion corrections have negligible effect. Gruszczynska et al., (2019) compared the joint environmental mass loading from atmospheric, hydrological and non-tidal ocean loading with the CME computed using International GNSS Service (IGS) stations in worldwide and Europe, respectively. However, Zhu et al. (2017) used the regional stacking approach for the CME extraction which has limitation for the large region. Although the spatio-temporal extraction of CME used by Gruszczynska et al., (2019) performed better than the regional stacking methods, it has limitations in the reliable extraction of CME for large regions. Despite some limitations, recent studies did provide insights in the relation of CME with the environmental mass loading.

In the present study, we test the relation of CME with the atmospheric mass loading (AML) 3-D displacement of the crust using data from Taiwan’s dense, continuous GPS stations across the island that provides proper opportunity to conduct such a study. The size of Taiwan island (394 km long and 144 km wide) assures a quality CME extraction, as the spatial coherence is likely to be high within 600 km distance range (Márquez-Azúa & DeMets, 2003; Williams et al., 2004), and the least variation in the large wavelength source such as AML, providing an optimal opportunity to test the relation of AML and CME. We shall implement the Empirical Orthogonal Function (EOF) analysis to extract the CME signal. We shall examine CME’s cross-correlation and coherence with the atmospheric mass loading (AML) 3-D

displacement of the crust, and conclude positively a dominant role of the AML in causing the CME, at least in Taiwan. The waveform analysis schemes such as cross-correlation and coherence provides more reliable estimates than just the variance reduction analysis employed by previous studies. We shall also compute the quantitative response of CME due to AML linear least-squares regression which is further assessed for the confidence of the model.

2 Data Preparation

2.1 Continuous GPS Data

We obtain the continuous GPS daily data from the GPS Lab of the Academia Sinica (Chen et al., 2013) that comprises Taiwan's local networks of the Central Weather Bureau, Academia Sinica, and Central Geological Survey. The GPS data are routinely compiled, processed by the means of Bernese software and solved relative to the tectonically stable station (S01R) of Penghu off the west coast (Chang & Chao, 2014; Chen et al., 2013; Yu et al., 1997). The International GPS Service final orbits and the standard antenna calibration were employed to reduce the effects of the orbit errors and the phase center biases. The GPS Lab processing mitigates the first-order ionospheric bias by forming the double-differenced ionosphere-free linear combination of carrier phase observations (Bos & Spakman, 2003; Chen et al., 2013; Yu et al., 1997).

In our study, we select data out of two hundred eighty-three available GPS stations in Taiwan observed for over 10 years and one hundred nine stations observed less than 10 years. Many of these stations have significant intermittent time gaps and hence unsuitable for this study. The application of EOF analysis requires complete dataset with no missing values. Several techniques have been developed to deal with data gaps. Shen et al. (2014) proposed the use of a modified PCA to interpolate the data gaps by minimizing the weighted quadratic norm of the Principal Component (PCs) unknowns. Li et al. (2015) filled the gap epoch with the available values from other stations, assuming spatially averaged initial residuals. These schemes fail when gaps occur with common epochs of observation in a network. Gruszczynski et al. (2019) introduced the probabilistic PCA method that is robust for dealing with data gaps and provide more reliable results. We select the 47 best time series stations (**Figure 1**a) based on the consistency, quality and data length from Jan 1, 2006, to Dec 31, 2015 (10-year span). We consider the records above the chosen threshold of 2σ of the mean variations as outliers and linearly-interpolate over the data gaps and average them to obtain the daily samplings. We ensure that the selected stations have continuous recordings with intermittent gaps of less than 5 days with cumulative gaps no more than 5%. We deselect the stations that are not characterized by any common observational epochs in the time series (see Figure S1 for the data availability at the selected stations). The average number of epochs of 47 selected stations is 3834 for 10 years compared to 4538 epochs used by Zhu et al. (2017) for 13.8 years. Selected stations (colored circles in **Figure 1**a) sample the whole of Taiwan reasonably well. The maximum distance between the two stations is 380 km, which is well within the 1000 km distance to obtain the good spatial correlations of the GPS residuals (Márquez-Azúa & DeMets, 2003). The timespan is essential in the estimation of reliable correlation between two time series. Santamaría-Gómez and Mémin (2015) found that at least 4 years of continuous data is important for the reliable

estimation of secular velocities. Chao and Chung (2019) demonstrated that sufficiently large degrees of freedom is crucial for finding the reliable correlation in both time and frequency domains. The 10-year long daily time series used in this study provide sufficient temporal resolution to reliably investigate the relationship of the extracted CME to the possible source of CME (Blewitt & Lavallee, 2002; Klos et al., 2015).

Figure 1(a) Topographical map of Taiwan displaying 392 available stations (shown by gray-filled circles) and 47 selected stations (colored circles) from the dense GPS array of Taiwan. The color of the selected stations shows the vertical component cross-correlation values of the given station with the arbitrarily chosen reference station SHJU (shown by the magenta star). The AML displacement data is retrieved at the station TAIW (shown by the white square). **(b)** (TOP) The time-variable standard deviation of the daily fluctuations of the GPS residuals for the three components for all the selected GPS stations exhibiting apparent seasonality. (BOTTOM) The calculated AML displacements (see text later) for the three components at TAIW. vertical: red, north: green, east: blue.

We apply the standard procedure to deterministically model each GPS time series $f(t)$, in three components (north, east, and vertical) independently, as a linear combination of the form:

$$f(t) = a + bt + \sum_{k} c_k H(t - t_0) + \sum_{k=1}^{7} \left[A_k cos(\frac{2\pi t}{P_k}) + B_k sin(\frac{2\pi t}{P_k}) \right] + residual \qquad (1)$$

where $a + bt$ accounts for the linear trends due to the "secular" tectonic motion, and the Heaviside function $H(t - t_0)$ account for all the vertical offsets on the known occurrence day t_0 mostly for coseismic deformation due to Taiwan's frequent earthquakes but also including instrument and antenna changes, or modification in analysis strategy. The seven pairs of periodic signals ($k = 1$ to 7) with amplitude A_k and B_k comprise two seasonal signals (annual, semiannual) plus four tidal signals (with periods 13.6608 days, Mf; 14.7653 days, Msf; 27.5546 days, Mm; 18.6 years) and a draconitic signal (with period 351.6 days). Although draconitic periods are difficult to resolve by the spectral analysis with timespan less than 25.6 years (Klos et al., 2019), previous studies suggest that draconitic signal contribute significantly to the overall data variance and should be mitigated prior to the CME extraction (Amiri-Simkooei, 2013; Blewitt & Lavallee, 2002). We then conduct a linear least-squares regression by minimizing the variance of the *residual*, and obtain the estimates for the unknown coefficients a, b, c, A_k, B_k for each 10-year GPS time series. We subtract the estimated terms to reveal the *residual* on the right side of Equation (1), hereinafter called GPS residuals, constituting the set of target time series to be analyzed below. The GPS residuals is thus the sum of the spatially correlated CME and random noises.

179 2.2 CME and the seasonality of the GPS residuals

180 Figure 1a presents the Pearson correlation coefficients (ρ) of all vertical component GPS
181 residuals series with the arbitrarily selected reference station SHJU having similar elevation as
182 most of the other stations, to assess the consistent and simultaneous spatial fluctuations across
183 the network. The color of the circles represents the ρs of all stations with SHJU. Given the 10-
184 year long, broad-band daily fluctuations with high statistical degrees of freedom, the expected
185 correlation of two random time series is 0 ± 0.04 as obtained in our Monte Carlo simulation test
186 (cf. Chao and Chung, 2019). So, we observe significant correlations among the GPS residuals for
187 the stations in Taiwan. As the maximum inter-station distance in the network is only 380 km, no
188 appreciable differences are seen in the correlation for farther stations than the nearer ones.

189

190 The apparent strong spatial coherence on timescales of weeks among GPS residuals of all
191 stations reflects the presence of CME in the region (Chang & Chao, 2014; Dong, Fang, Bock,
192 Cheng, & Miyazaki, 2002a; Mao et al., 1999; Márquez-Azúa & DeMets, 2003; Tiampo et al.,
193 2004; Wdowinski et al., 2004; Williams et al., 2004). We segregate the GPS network stations
194 into west and east to differentiate any possible direct effect of the meteorological difference on
195 the two opposite coasts of Taiwan (Figure S2). We do not find any quantifiable difference in the
196 fluctuations among them.

197

198 The time-variable standard deviation of the envelope of the daily fluctuations of all the
199 GPS residuals series (**Figure 1**b) exhibits a significant seasonality in all three components
200 (Chang & Chao, 2014; Dong et al., 2006). The fluctuation during summertime is nearly two-fold
201 of the wintertime's. This implies CME's meteorology-related origin. The horizontal components
202 are less variant than the vertical by a factor of 2-3, indicating that the CME is strongly sensitive
203 to vertical phenomena.

204

205 The Kaiser-Meyer-Olkin (KMO) Test statistically measures the suitability of selected
206 GPS residuals to efficiently extract the CME using multivariate analysis such as EOF by
207 estimating the proportion of variance among all the observed variables (Cerny & Kaiser, 1977;
208 Gruszczynski et al., 2019; Hill, 2011; Santos et al., 2014). The resulting KMO index ranges from
209 0 and 1 where values close to 1 represents significant variance among the observed variables. For
210 the observation matrix of our 47 selected GPS residual time series, the KMO index is 0.95, 0.99,
211 0.99 for the vertical, north and east components, respectively. These high index values suggest
212 the presence of good quality of spatial correlation in the data in addition to the direct
213 measurement of correlation coefficients among the stations and enables us to proceed with the
214 extraction of CME.

215

216 2.3 Atmospheric mass loading (AML) data

217 We obtain the calculated AML displacement (in units of mm) for all three components
218 from the webpage of the International Mass Loading Service[1] (Dobslaw et al., 2017; Petrov,

[1] http://massloading.net

2015; Petrov & Boy, 2004; Rienecker et al., 2008) , which maintains the AML displacement time series induced for 1272 space geodesy sites worldwide from 1976.01.01 to the present in EPHEDISP format. They are derived from the surface pressure fields from the National Centers for Environmental Prediction (NCEP) Reanalysis numerical weather model at $2.5^\circ \times 2.5^\circ$ grid with 6-hour time resolution (Kalnay et al., 1996). The root-mean square difference between this model and the observed mass loading is typically around 5% (Petrov & Boy, 2004; Velicogna et al., 2001).

We simply download the pre-computed 3-D AML displacement time series at the station TAIW (121.5365°, 24.8742°, 44.0 m) out of the two available locations in Taiwan. We average the 6-hourly samples to obtain the daily values to match the GPS daily sampling. We, again, conduct the least-squares fitting of the AML displacement time series to remove the linear trend and the seasonal signals as in Equation (1) to retrieve the non-linear, non-seasonal AML displacement, or the AML residuals.

3 Results

Our task is to first extract the CME part of the signal from the GPS residuals and then compare quantitatively the CME with the AML residuals to reveal their inter-relationship.

3.1 EOF of GPS residuals to extract CME

The EOF, a form of PCA, decomposes the space-time observations into a set of orthogonal spatial patterns along with a corresponding set of orthogonal time series (Fukuoka, 1951; Hannachi et al., 2007; Lorenz, 1956; Menke, 2018). We construct the space-time data matrix $\boldsymbol{D}(t_i, x_j)$ of the GPS residuals where $i = 1, 2, \ldots, 3652$ stands for the daily time tag for 10 years, and $j = 1, 2, \ldots, 47$ for the selected stations. EOF retrieves the coherent spatio-temporal signals mathematically by solving for a series of eigenmodes of the covariance matrix, $\boldsymbol{D}^T\boldsymbol{D}$, expressed in standing oscillations in the form of the product of spatial pattern and time series, $S_k(x) \cdot T_k(t)$ for a given target region and selected timespan, with mode index $k = 1, 2, \ldots$ (Chang & Chao, 2014; Chao & Liau, 2019). The spatial pattern $S_k(x)$ is the *k*th eigenvector solution and the time series $T_k(t)$ is the projection of the data matrix onto the spatial pattern obtained by the inner product $\boldsymbol{D} \cdot S_k(x)$. We arrange the eigenmodes in decreasing order of (the positive) eigenvalues, such that the first eigenmode represents the biggest contributor to the variance (measured by the ratio of the eigenvalue for the given mode index to the sum of all eigenvalues) of the GPS residuals. Here we expect that the first mode is for the CME, while the higher modes reflect secondary effects or local and short-period signals or noises not of interest here. This is consistent with previous studies (Dong et al., 2006; Gruszczynski et al., 2019; Y. Shen et al., 2014). The calculated eigenvalue spectrum of the EOF along with their standard errors (calculated using Monte Carlo simulations) shows that the first mode is nondegenerate and separated from the rest.

Figure 2 shows the first two modes solved for the 47 selected GPS residual records for 10 years, each given in terms of spatial (S, linearly interpolated at 0.01 degrees) and corresponding time series (T, daily). We normalize the spatial pattern $S_k(x)$ for the first mode by dividing with the RMS value (given that it is near-uniform in space), whereas for the second mode by dividing with the standard deviation (given its fluctuation around 0). The corresponding time series, or principal components, are scaled by multiplying by the same normalization value, transferring the magnitude information of eigenvectors into the principal components, which hence has the same unit as the data (mm in our study). The first EOF mode captures 56% of the vertical, 75% of the north, and 63% of the east component variances, whereas the second mode captures only 7%, 4%, and 9% variance, respectively. The relatively high variance in the north component than the east and vertical is because of the higher spatial correlation of the north (Amiri-Simkooei, 2013; Williams et al., 2004).

Figure 2 The first two EOF modes of the GPS residuals. The columns correspond to the three components - U, N and E. The **upper panel** shows the spatial and temporal pattern of the Mode 1; the **lower panel** those of Mode 2. The spatial pattern of the first mode is normalized by its RMS value, whereas the second mode by its standard deviation.

3.2 Comparison of CME with the AML residuals

Figure 3a compares the extracted CME signal in the form of the EOF mode 1 with the AML residuals time series alongside each other. They oscillate in-phase for the U, N and E components. The scatter of CME solutions is 2-3 folds greater than the AML residuals for the U component (Petrov & Boy, 2004).

The calculated cross-correlation function of CME with respect to time-shifted copies of AML residuals (**Figure 3**b) shows the striking correlation around the zero time lag. The ρ for the U components of CME and AML residuals is 0.43 while that of N and E components are 0.19 and 0.21, respectively. For reference, the probability of an uncorrelated system producing datasets that have a ρ of 0.43 is extremely minimal (nominal p-value of the order 10^{-162}) (Granger & Newbold, 2014). Furthermore, we conduct the cross-correlation of the three CME components among themselves (Figure S3). The ρs between the vertical and horizontal components are significantly low, while that of the two horizontal components is significantly high (significance evaluated by Monte Carlo tests).

Additionally, we calculate the Lin's concordance correlation coefficient (ρ_c) that is based on covariation and correspondence between two sets of scores in contrast to the linear covariation for the ρ (Gruszczynski et al., 2019; Lin, 1989; Tian & Shen, 2016). Unlike ρ that measures how far the data points are from the line, the ρ_c evaluates the joint deviation of the data points from a 45-degree line through the origin representing perfect agreement. We use this

metric to quantify the agreement (degree of concordance) between the CME and AML time series. We find the ρ_c values of 0.33, 0.19, 0.18 for the vertical, north and east components, respectively. The value of 0.33 for the vertical component suggests that the variations in CME are in ~33% agreement with AML. It should be emphasized that the ρ_c value is always less than the ρ value because ρ_c is not exact linear correlation between two continuous variables and only estimate the degree to which the pairs fall on the 45-degree line intersecting the origin (intercept of 0).

Figure 3 Comparison of AML residuals variations with the CME. **(a)** Plot of the vertical, north and east components of AML residuals (red) and CME (blue) signals. **(b)** Cross-correlation of CME with the AML residuals displacement for all three components. CME time series is correlated with AML residuals. **(c)** Magnitude-squared coherence (TOP) and phase spectrum (MIDDLE) between the vertical component CME and AML residuals time series, normalized Lomb-Scargle periodogram w.r.t the standard deviation (BOTTOM)

Besides, the frequency dependence between two time series at different time scales can be quantified by calculating the complex cross-coherence spectra (Båth, 2012; Stoica & Moses, 2005). **Figure 3**c shows the coherence spectra of the U component time series of CME and AML residual in terms of the coherence magnitude spectrum and coherence phase computed using the multitaper technique (Chao & Chung, 2019; Chao & Eanes, 1995; Thomson, 1982). Notice the high coherence concentrated in the spectral band of 11 - 14 cycles per year (cpy; 26 - 33 days per cycle) with corresponding phase spectrum at near zero. The fraction of the integrated power between 11 - 14 cycles for U component CME and AML residuals is 10% and 13% of the total power, respectively. The significance of the strong coherence for frequency higher than 20 cpy is uncertain because the underlying power spectrum at these periods for both vertical component CME and AML residuals is fairly small (<1% of total power). The power and coherence spectrum for north and east components are presented in Supporting Information (see Figure S5).

Unlike Fourier analysis, wavelet analysis provides more localized temporal (or spatial) and frequency information (Chao et al., 2014). We calculate the continuous wavelet spectrum of the CME and AML residuals time series to compare the two signals; they look very similar to each other, particularly at longer periods. These are present in Supporting Information (Figure S4).

As the correlation function only takes into account the normalized measure of the waveform pattern, we need an estimate of the relative amplitude between the AML and GPS residuals. We establish the linear regression relation such that the $GPS\ resd$ are a product $A * AML\ resd$ where the unknown proportional constant A is hereinafter called admittance factor (Petrov & Boy, 2004).

$$\boldsymbol{GPS\,resd} = \boldsymbol{A} * \boldsymbol{AML\,resd} + \boldsymbol{noise} \qquad \mathbf{2}$$

The variation in the estimated admittance factor at each station across the GPS network in Taiwan is close to 1 (see Figure S6 in Supporting Information). The direct admittance factor of AML residuals and extracted CME from the GPS residuals is 0.93 indicating the strong relationship of CME and AML residuals. We find the *p*-value (95% confidence interval) of the AML residuals to be nominally as small as 8.35×10^{-168}, confirming the existence of definite relationship between the AML residuals and CME. To evaluate the overall fit of the model, we calculated the *R*-squared value, which is the proportion of variance in the observed data that can be explained by the model. The *R*-squared value for the linear regression model between AML residuals and the CME is 0.19. The summary of the regression analysis is shown in Figure S7 in the Supporting Information.

4 Discussion and Conclusions

Before we conduct our CME-AML correlation-coherence studies, there are already several considerations that would corroborate the notion of AML cause for CME: (i) the evident seasonality in the strength of GPS residual standard deviation (Figure 1b); (ii) the dominance of the effect in vertical over horizontals; (iii) the CME spatial pattern matching the topography (Figure 2); (iv) the "breathing" behavior of CME (Figure 2) as the AML is of large spatial scale in general. We find a significant time-domain correlation of 0.43 between the CME and AML residuals for the vertical fluctuations (**Figure 2**b). Coherence amplitude (**Figure 2**c [TOP]) and phase (**Figure 2**c [MIDDLE]) results along with the periodogram (**Figure 2**c [BOTTOM]) indicate that the CME is predominantly influenced by AML on the monthly timescale or the frequency band of 11-14 cpy with latency less than a day. The estimated admittance factor of 0.9x between CME and AML using the least-squares regression tells us that up to 90% of the vertical component CME amplitudes can be accounted for by the AML residuals.

We apply EOF analysis to efficiently extract CME from the GPS residuals by breaking it into series of orthogonal modes. The near-uniform amplitude of the first mode's spatial pattern illustrates the in-phase "breathing" motion, signifying the CME that follows the corresponding PC temporal variation. The slight deviation from uniformity of the spatial amplitude at the topographically elevated and lower regions reveals that the CME shows nearly same spatial amplitude variation for the similarly elevated regions of the study area. If we compensate the CME's spatial pattern for the differences in topography, then relative variations in the spatial amplitude will be significantly diminished (not shown). The coherent variation in CME's spatial amplitude and apparent topography can likely be a result of AML on the CME since the AML varies strongly with elevation (Tregoning & van Dam, 2005; van Dam et al., 2010). The near uniform spatial variations of CME is also consistent with the notion of a large wavelength AML source found by Dong et al. (2006).

In comparison, the second mode's spatial amplitude undulates notably and contributes only up to 7 % of the total variance for the vertical component. The temporal variations for the

mode 2's three components' temporal variations over the 10 years display some systematic structure (**Figure 2** lower panel), indicating the essential relationship with some geophysical phenomena. We find, perhaps not surprisingly, the high correlation for all three components of the second mode of EOF with the global dynamic climatic changes associated with tropical stratospheric circulation - El Niño–Southern Oscillation (ENSO) and Pacific Decadal Oscillation (PDO) (see Figure S8 in Supporting Information for the correlation results). ENSO is the strongest interannual perturbation to the climate system and is associated with a strong re-distribution of heat, especially in the Pacific Ocean. The "recharge-discharge oscillator", where the equatorial ocean accumulates heat prior to El Niño and depletes it during and after El Niño (Cane & Zebiak, 1985; Wyrtki, 1975), set up the time scale of ENSO (Jin & Jin, 1997). PDO is the reddened response to both atmospheric noise and ENSO and hence results in more decadal variability than either (Mantua & Hare, 2002; Newman et al., 2003). The strong correlation of PDO and ENSO with the EOF second mode may be related to their strong dependence on all timescales (Newman et al., 2003). The correlation of EOF 2 is shifted nominally in time by 16 months for the vertical and north component, while 4 months for the east component from the ENSO, which may be the manifestation of the recharge-discharge oscillation. Further studies are required to establish the causal relationship between the ENSO/PDO and GPS fluctuations.

We find that the vertical CME variations explain 56% of the variance in the GPS residuals that are strongly correlated to the AML variations in Taiwan. The north and east component CME explain significantly higher variance in the GPS residuals, however, the correlation with the corresponding components of AML is considerably low. Since Taiwan is an island, the CME variations (mainly in the horizontal components) may additionally be related to the crustal response of hydrological load and non-tidal oceanic load variations (Bettinelli et al., 2008). It is crucial to study and assess their contribution in relation to CME oscillations. There could be other minor physical and nonphysical factors that can possibly have influence on the CME such as tropospheric water vapor, bedrock thermal expansion, phase center variation models, thermal noise of the antenna, environmental effects near the antenna (more common in humid tropics), local multi-path, mismodeled satellite orbits, reference frame limitations, etc. and is not regarded in this study (Dixon & Wolf, 1990; Dong, Fang, Bock, Cheng, & Miyazaki, 2002a; Mao et al., 1999; Miyazaki et al., 2003; Prawirodirdjo et al., 2006; Wdowinski et al., 1997).

The correlation coefficient value of 0.43 is significantly high for the broad-band vertical data of length 10 years (Chao & Chung, 2019). It strongly suggests that the AML influences the CME in the vertical GPS data of Taiwan. The uncorrelated vertical and horizontal components of CME signify no effect of the CME horizontal fluctuations on the AML fluctuations that is correlated with vertical CME fluctuations. Using the EOF analysis, we estimate ~54% of the vertical GPS residuals' fluctuations are CME, and the fraction is much larger for the horizontal components. In the absence of any significant tectonic processes and strong local effects in a region, up to ~50% of vertical CME can be attributed to the AML residuals judging from the estimate of the fraction of variance present in the first mode EOF and the admittance factor. This estimate agrees with the ~60% of atmospheric mass loading contributions evident from the GPS vertical position measurements (for 19 global stations) estimated by van Dam et al., (1994). Our

results also agrees with the recent study of Gruszczynska et al. (2019) for the overall reduction of 68% for 229 global stations when compared to the environmental mass loading models.

Our results are constrained by the quality of the data obtained from the NCEP Reanalysis. The typical misfit of 5% between the observed and modeled AML can potentially affect the results (Petrov & Boy, 2004). The 2.5° spatial resolution limit of the obtained data, even after applying the land-sea mask of 0.25° resolution, may also not have sufficiently modeled the atmospheric loading field at the station TAIW (nearly 1.5° from the coast). This error is 2-3 times larger for the horizontal components than the vertical, that being so we have focused on the results for the vertical component only. Also, several previous studies (Gruszczynska et al., 2019; Zhu, Zhou, & Liu, 2017) suggest the significantly larger effect of vertical components on CME than the horizontals. Since our initial dataset features some missing values that was filled using the interpolation schemes, we expect some implicit error (maximum of 10%) in our computed CME (Gruszczynski et al., 2019).

Understanding the relation of CME with the atmospheric mass loading is critical for extending various spatial filtering methods to extensive networks. It can potentially enhance the precision of the models that are required in the routine analysis of geodetic observations. The knowledge of GPS noise content is essential in the estimation and assignment of realistic uncertainties to the parameters estimated from them. Comprehension of the origin and source of CME is valuable in classifying noise components, which affects the resulting rate uncertainties and hence the derivation of crustal motion models. Our study also suggests an alternative of constricting the effect of CME by removing the effects of atmospheric mass loading from the continuous GPS data.

Acknowledgments

The GPS data used in this work are available from the GPS Lab website (http://gps.earth.sinica.edu.tw) of the Institute of Earth Sciences, Academia Sinica of Taiwan. The Atmospheric pressure loading displacement dataset for TAIW is obtained from the International Mass Loading Service website (http://massloading.net) maintained by Leonid Petrov. We also thank W. J. Cheng for initial numerical tests of the data.

References

Amiri-Simkooei, A. R. (2013). On the nature of GPS draconitic year periodic pattern in multivariate position time series. *Journal of Geophysical Research: Solid Earth*, *118*(5), 2500–2511. https://doi.org/10.1002/jgrb.50199

Båth, B. M. (2012). Spectral Analysis in Geophysics. Elsevier.

Bettinelli, P., Avouac, J.-P., Flouzat, M., Bollinger, L., Ramillien, G., Rajaure, S., & Sapkota, S. (2008). Seasonal variations of seismicity and geodetic strain in the Himalaya induced by surface hydrology. *Earth and Planetary Science Letters*, *266*(3-4), 332–344.

Blewitt, G., & Lavallee, D. (2002). Effect of annual signals on geodetic velocity. *Journal of Geophysical Research: Solid Earth*, *107*(B7), ETG 9–1–ETG 9–11. https://doi.org/10.1029/2001JB000570

Blewitt, G., Kreemer, C., Hammond, W. C., & Goldfarb, J. M. (2013). Terrestrial reference frame NA12 for crustal deformation studies in North America. *Journal of Geodynamics*, *72*, 11–24. https://doi.org/10.1016/j.jog.2013.08.004

Bock, Y., Prawirodirdjo, L., & Melbourne, T. I. (2004). Detection of arbitrarily large dynamic ground motions with a dense high-rate GPS network, *31*(6), n/a–n/a. https://doi.org/10.1029/2003GL019150

Bos, A. G., & Spakman, W. (2003). Surface deformation and tectonic setting of Taiwan inferred from a GPS velocity field, *108*(B10), 77. https://doi.org/10.1029/2002JB002336

Cane, M. A., & Zebiak, S. E. (1985). A Theory for El Niño and the Southern Oscillation, *228*(4703), 1085–1087. https://doi.org/10.7916/D8C2562D

Cerny, B. A., & Kaiser, H. F. (1977). A study of a measure of sampling adequacy for factor-analytic correlation matrices. *Multivariate Behavioral Research*, *12*(1), 43–47.

Chang, E. T. Y., & Chao, B. F. (2014). Analysis of coseismic deformation using EOF method on dense, continuous GPS data in Taiwan. *Tectonophysics*, *637*(C), 106–115. https://doi.org/10.1016/j.tecto.2014.09.011

Chao, B. F., & Chung, C. H. (2019). On Estimating the Cross Correlation and Least Squares Fit of One Data Set to Another With Time Shift. *Earth and Space Science*, *6*(8), 1409–1415. https://doi.org/10.1029/2018EA000548

Chao, B. F., & Eanes, R. (1995). Global gravitational changes due to atmospheric mass redistribution as observed by the Lageos nodal residual. *Geophysical Journal International*, *122*(3), 755–764.

Chao, B. F., & Liau, J. R. (2019). Gravity Changes Due to Large Earthquakes Detected in GRACE Satellite Data via Empirical Orthogonal Function Analysis. *Journal of Geophysical Research: Solid Earth*, *124*(3), 3024–3035. https://doi.org/10.1029/2018JB016862

Chao, B. F., Chung, W., Shih, Z., & Hsieh, Y. (2014). Earth's rotation variations: A wavelet analysis. *Terra Nova*, *26*(4), 260–264.

Chen, H.-Y., Lee, J.-C., Tung, H., Yu, S.-B., Hsu, Y.-J., & Lee, H. (2013). A New Velocity Field from a Dense GPS Array in the Southernmost Longitudinal Valley, Southeastern Taiwan, *24*, 837–862. https://doi.org/10.3319/TAO.2013.06.18.01(T)

Ching, K.-E., Rau, R.-J., Lee, J.-C., & Hu, J.-C. (2007). Contemporary deformation of tectonic escape in SW Taiwan from GPS observations, 1995–2005. *Earth and Planetary Science Letters*, *262*(3-4), 601–619. https://doi.org/10.1016/j.epsl.2007.08.017

Dixon, T. H., & Wolf, S. K. (1990). Some tests of wet tropospheric calibration for the CASA Uno Global Positioning System experiment, *17*(3), 203–206.

Dobslaw, H., Bergmann-Wolf, I., Dill, R., Poropat, L., Thomas, M., Dahle, C., et al. (2017). A new high-resolution model of non-tidal atmosphere and ocean mass variability for de-aliasing of satellite gravity observations: AOD1B RL06. *Geophysical Journal International*, *211*(1), 263–269.

Dong, D., Fang, P., Bock, Y., Cheng, M. K., & Miyazaki, S. (2002a). Anatomy of apparent seasonal variations from GPS-derived site position time series, *107*(B4), ETG 9–1–ETG 9–16. https://doi.org/10.1029/2001JB000573

Dong, D., Fang, P., Bock, Y., Cheng, M. K., & Miyazaki, S. (2002b). Anatomy of apparent seasonal variations from GPS-derived site position time series. *Journal of Geophysical Research: Solid Earth*, *107*(B4), ETG–9.

Dong, D., Fang, P., Bock, Y., Webb, F., Prawirodirdjo, L., Kedar, S., & Jamason, P. (2006). Spatiotemporal filtering using principal component analysis and Karhunen-Loeve expansion approaches for regional GPS network analysis. *Journal of Geophysical Research: Solid Earth*, *111*(B3), n/a–n/a. https://doi.org/10.1029/2005JB003806

Dragert, H., Wang, K., & James, T. S. (2001). A Silent Slip Event on the Deeper Cascadia Subduction Interface. *Science*, *292*(5521), 1525–1528. https://doi.org/10.1126/science.1060152

Fukuoka, A. (1951). The Central Meteorological Observatory, A study on 10-day forecast (A synthetic report). *Geophysical Magazine*, *22*(3), 177–208.

Granger, C. W. J., & Newbold, P. (2014). Forecasting economic time series.

Gruszczynska, M., Rosat, S., Klos, A., Gruszczynski, M., & Bogusz, J. (2019). Multichannel Singular Spectrum Analysis in the Estimates of Common Environmental Effects Affecting GPS Observations. In *Geodynamics and Earth Tides Observations from Global to Micro Scale* (pp. 211–228). Cham: Birkhäuser, Cham. https://doi.org/10.1007/978-3-319-96277-1_17

Gruszczynski, M. (2016). Orthogonal transformation in extracting of common mode error from continuous GPS network. *Acta Geodynamica Et Geomaterialia*, 291–298. https://doi.org/10.13168/AGG.2016.0011

Gruszczynski, M., Klos, A., & Bogusz, J. (2019). A Filtering of Incomplete GNSS Position Time Series with Probabilistic Principal Component Analysis. In C. Braitenberg, G. Rossi, & G. A. E. T. E. group (Eds.), *Geodynamics and Earth Tides Observations from Global to Micro Scale* (pp. 247–273). Cham: Springer International Publishing.

Hannachi, A., Jolliffe, I. T., & Stephenson, D. B. (2007). Empirical orthogonal functions and related techniques in atmospheric science: A review. *International Journal of Climatology*, *27*(9), 1119–1152. https://doi.org/10.1002/joc.1499

Hatanaka, Y., Sawada, M., Horita, A., Kusaka, M., Johnson, J. M., & Rocken, C. (2014). Calibration of antenna-radome and monument-multipath effect of GEONET—Part 2: Evaluation of the phase map by GEONET data. *Earth, Planets and Space*, *53*(1), 23–30. https://doi.org/10.1186/BF03352359

Heki, K., Otsuka, Y., Choosakul, N., Hemmakorn, N., Komolmis, T., & Maruyama, T. (2006). Detection of ruptures of Andaman fault segments in the 2004 great Sumatra earthquake with coseismic ionospheric disturbances. *Journal of Geophysical Research: Solid Earth*, *111*(B9), 1133. https://doi.org/10.1029/2005JB004202

Hill, B. D. (2011). Sequential Kaiser-meyer-olkin Procedure as an Alternative for Determining the Number of Factors in Common-factor Analysis: a Monte Carlo Simulation.

Hudnut, K. W., King, N. E., Galetzka, J. E., Stark, K. F., Behr, J. A., Aspiotes, A., et al. (2002). Continuous GPS Observations of Postseismic Deformation Following the 16 October 1999 Hector Mine, California, Earthquake (Mw 7.1). *Bulletin of the Seismological Society of America*, *92*, 1403–1422. https://doi.org/10.1785/0120000912

Jin, F.-F., & Jin, F.-F. (1997). An Equatorial Ocean Recharge Paradigm for ENSO. Part I: Conceptual Model. *Http://Dx.Doi.org/10.1175/1520-0469(1997)0542.0.CO;2*, *54*(7), 811–829. https://doi.org/10.1175/1520-0469(1997)054<0811:AEORPF>2.0.CO;2

Johansson, J. M., Davis, J. L., Scherneck, H. G., Milne, G. A., Vermeer, M., Mitrovica, J. X., et al. (2002). Continuous GPS measurements of postglacial adjustment in Fennoscandia 1. Geodetic results. *Journal of Geophysical Research: Solid Earth*, *107*(B8), ETG 3–1–ETG 3–27. https://doi.org/10.1029/2001JB000400

Kalnay, E., Kanamitsu, M., Kistler, R., Collins, W., Deaven, D., Gandin, L., et al. (1996). The NCEP/NCAR 40-year reanalysis project. *Bulletin of the American Meteorological Society*, *77*(3), 437–472.

King, M. A., Altamimi, Z., Boehm, J., Bos, M., Dach, R., Elosegui, P., et al. (2010). Improved Constraints on Models of Glacial Isostatic Adjustment: A Review of the Contribution of Ground-Based Geodetic Observations. *Surveys in Geophysics*, *31*(5), 465–507. https://doi.org/10.1007/s10712-010-9100-4

Klos, A., Bogusz, J., Figurski, M., & Gruszczynski, M. (2015). Error analysis for European IGS stations. *Studia Geophysica Et Geodaetica*, *60*(1), 17–34. https://doi.org/10.1007/s11200-015-0828-7

Klos, A., Gruszczynska, M., Bos, M. S., Boy, J. P., & Bogusz, J. (2019). Estimates of vertical velocity errors for IGS ITRF2014 stations by applying the improved singular spectrum analysis method and environmental loading models. In *Geodynamics and Earth Tides Observations from Global to Micro Scale* (pp. 229–246). Springer.

Larson, K. M., Bodin, P., & Gomberg, J. (2003). Using 1-Hz GPS Data to Measure Deformations Caused by the Denali Fault Earthquake. *Science*, *300*(5624), 1421–1424. https://doi.org/10.1126/science.1084531

Li, W., Shen, Y., & Li, B. (2015). Weighted spatiotemporal filtering using principal component analysis for analyzing regional GNSS position time series. *Acta Geodaetica Et Geophysica*, *50*(4), 419–436.

Lin, L. I.-K. (1989). A Concordance Correlation Coefficient to Evaluate Reproducibility. *Biometrics*, *45*(1), 255. https://doi.org/10.2307/2532051

Lorenz, E. N. (1956). Empirical orthogonal functions and statistical weather prediction.

Malet, J. P., Maquaire, O., & Calais, E. (2002). The use of Global Positioning System techniques for the continuous monitoring of landslides: application to the Super-Sauze earthflow (Alpes-de-Haute-Provence, France). *Geomorphology*, *43*(1-2), 33–54. https://doi.org/10.1016/S0169-555X(01)00098-8

Mantua, N. J., & Hare, S. R. (2002). The Pacific Decadal Oscillation. *Journal of Oceanography*, *58*, 35–44.

Mao, A., Harrison, C. G., & Dixon, T. H. (1999). Noise in GPS coordinate time series, *104*(B2), 2797–2816.

Massonnet, D., Thatcher, W., & Vadon, H. (1996). Detection of postseismic fault-zone collapse following the Landers earthquake. *Nature*, *382*(6592), 612–616. https://doi.org/10.1038/382612a0

Márquez-Azúa, B., & DeMets, C. (2003). Crustal velocity field of Mexico from continuous GPS measurements, 1993 to June 2001: Implications for the neotectonics of Mexico, *108*(B9), 21,943–20. https://doi.org/10.1029/2002JB002241

Melbourne, T. I., & Webb, F. H. (2002). Precursory transient slip during the 2001 Mw = 8.4 Peru earthquake sequence from continuous GPS, *29*(21), 28–1–28–4. https://doi.org/10.1029/2002GL015533

Menke, W. (2018). Geophysical Data Analysis. Academic Press.

Miller, M. M., Melbourne, T., Johnson, D. J., & Sumner, W. Q. (2002). Periodic Slow Earthquakes from the Cascadia Subduction Zone. *Science*, *295*(5564), 2423–2423. https://doi.org/10.1126/science.1071193

Miyazaki, S., Iwabuchi, T., Heki, K., & Naito, I. (2003). An impact of estimating tropospheric delay gradients on precise positioning in the summer using the Japanese nationwide GPS array. *Journal of Geophysical Research: Solid Earth*, *108*(B7), 5019. https://doi.org/10.1029/2000JB000113

Newman, M., Compo, G. P., & Alexander, M. A. (2003). ENSO-Forced Variability of the Pacific Decadal Oscillation. *Journal of Climate*, *16*, 1–5.

Petrov, L. (2015). The international mass loading service. In *REFAG 2014* (pp. 79–83). Springer.

Petrov, L., & Boy, J. P. (2004). Study of the atmospheric pressure loading signal in very long baseline interferometry observations. *Journal of Geophysical Research: Solid Earth*, *109*(B3), 409. https://doi.org/10.1029/2003JB002500

Prawirodirdjo, L., Ben Zion, Y., & Bock, Y. (2006). Observation and modeling of thermoelastic strain in Southern California Integrated GPS Network daily position time series. *Journal of Geophysical Research: Solid Earth*, *111*(B2), n/a–n/a. https://doi.org/10.1029/2005JB003716

Rienecker, M. M., Suarez, M. J., Todling, R., Bacmeister, J., Takacs, L., Liu, H. C., et al. (2008). The GEOS-5 Data Assimilation System: Documentation of Versions 5.0. 1, 5.1. 0, and 5.2. 0.

Santamaría-Gómez, A., & Mémin, A. (2015). Geodetic secular velocity errors due to interannual surface loading deformation. *Geophysical Journal International*, *202*(2), 763–767.

Santos, G., Costa, B., & Leal, A. (2014). Motivation and benefits of implementation and certification according ISO 9001 – the Portuguese experience. *International Journal of Engineering, Science and Technology*, *6*(5), 1–12.

Serpelloni, E., Faccenna, C., Spada, G., Dong, D., & Williams, S. D. P. (2013). Vertical GPS ground motion rates in the Euro-Mediterranean region: New evidence of velocity gradients at different spatial scales along the Nubia-Eurasia plate boundary. *Journal of Geophysical Research: Solid Earth*, *118*(11), 6003–6024. https://doi.org/10.1002/2013JB010102

Shen, Y., Li, W., Xu, G., & Li, B. (2014). Spatiotemporal filtering of regional GNSS network's position time series with missing data using principle component analysis. *Journal of Geodesy*, *88*(1), 1–12.

Smith, K. D., Seggern, von, D., Blewitt, G., Preston, L., Anderson, J. G., Wernicke, B. P., & Davis, J. L. (2004). Evidence for Deep Magma Injection Beneath Lake Tahoe, Nevada-California. *Science*, *305*(5688), 1277–1280. https://doi.org/10.1126/science.1101304

Stoica, P., & Moses, R. L. (2005). Spectral analysis of signals.

Teferle, F. N., Bingley, R. M., Williams, S. D. P., Baker, T. F., & Dodson, A. H. (2006). Using continuous GPS and absolute gravity to separate vertical land movements and changes in sea-level at tide-gauges in the UK. *Philosophical Transactions of the Royal Society a: Mathematical, Physical and Engineering Sciences*, *364*(1841), 917–930. https://doi.org/10.1098/rsta.2006.1746

Thomson, D. J. (1982). Spectrum estimation and harmonic analysis. *Proceedings of the IEEE*, *70*(9), 1055–1096.

Tiampo, K. F., Rundle, J. B., Klein, W., Ben-Zion, Y., & McGinnis, S. (2004). Using Eigenpattern Analysis to Constrain Seasonal Signals in Southern California. In *Computational Earthquake Science Part I* (Vol. 82, pp. 1991–2003). Basel: Birkhäuser, Basel. https://doi.org/10.1007/978-3-0348-7873-9_13

Tian, Y., & Shen, Z.-K. (2016). Extracting the regional common-mode component of GPS station position time series from dense continuous network. *Journal of Geophysical Research: Solid Earth*, *121*(2), 1080–1096. https://doi.org/10.1002/2015JB012253

Tregoning, P., & van Dam, T. (2005). Atmospheric pressure loading corrections applied to GPS data at the observation level, *32*(22), n/a–n/a. https://doi.org/10.1029/2005GL024104

van Dam, T., Altamimi, Z., Collilieux, X., & Ray, J. (2010). Topographically induced height errors in predicted atmospheric loading effects, *115*(B7), B09401–10. https://doi.org/10.1029/2009JB006810

vanDam, T. M., & Herring, T. A. (1994). Detection of atmospheric pressure loading using very long baseline interferometry measurements. *Journal of Geophysical Research: Solid Earth*, *99*(B3), 4505–4517. https://doi.org/10.1029/93JB02758

vanDam, T. M., Blewitt, G., & Heflin, M. B. (1994). Atmospheric pressure loading effects on Global Positioning System coordinate determinations, *99*, 23–939–23–950. https://doi.org/10.1002/jgrb.v99.B12;page:string:Article/Chapter

Velicogna, I., Wahr, J., & Van den Dool, H. (2001). Can surface pressure be used to remove atmospheric contributions from GRACE data with sufficient accuracy to recover hydrological signals?, *106*(B8), 16415–16434. https://doi.org/10.1029/2001JB000228

Wdowinski, S., Bock, Y., Baer, G., Prawirodirdjo, L., Bechor, N., Naaman, S., et al. (2004). GPS measurements of current crustal movements along the Dead Sea Fault. *Journal of Geophysical Research: Solid Earth*, *109*(B5), 1. https://doi.org/10.1029/2003JB002640

Wdowinski, S., Bock, Y., Zhang, J., Fang, P., & Genrich, J. (1997). Southern California permanent GPS geodetic array: Spatial filtering of daily positions for estimating coseismic and postseismic displacements induced by the 1992 Landers earthquake, *102*(B8), 18057–18070. https://doi.org/10.1029/97JB01378

Williams, S. D. P., Bock, Y., Fang, P., Jamason, P., Nikolaidis, R. M., Prawirodirdjo, L., et al. (2004). Error analysis of continuous GPS position time series. *Journal of Geophysical Research: Solid Earth*, *109*(B3), 333. https://doi.org/10.1029/2003JB002741

Wyrtki, K. (1975). El Niño—the dynamic response of the equatorial Pacific Oceanto atmospheric forcing. *Journal of Physical Oceanography*, *5*. https://doi.org/10.1175/1520-0485(1975)005<0572:ENTDRO>2.0.CO;2

Yu, S.-B., Chen, H.-Y., & Kuo, L.-C. (1997). Velocity field of GPS stations in the Taiwan area. *Tectonophysics*, *274*(1-3), 41–59. https://doi.org/10.1016/S0040-1951(96)00297-1

Yuan, L. G., DING, X. L., CHEN, W., KWOK, S., CHAN, S. B., HUNG, P. S., & CHAU, K. T. (2008). Characteristics of daily position time series from the Hong Kong GPS fiducial network. *Chinese Journal of Geophysics*, *51*(5), 976–990.

Zhang, H., Kuang, C., & Lu, C. (2016). Extract Common-Mode Error in Middle-Scale GPS Network Using Principal Component Analysis. In *China Satellite Navigation Conference (CSNC) 2016 Proceedings: Volume I* (Vol. 388, pp. 371–379). Singapore: Springer Singapore. https://doi.org/10.1007/978-981-10-0934-1_33

Zhu, Z., Zhou, X., & Liu, J. (2017). Noise analysis of common mode error in CMONOC GPS coordinate time series (pp. 190–193). Presented at the 2017 Forum on Cooperative Positioning and Service (CPGPS), IEEE. https://doi.org/10.1109/CPGPS.2017.8075122

Zhu, Z., Zhou, X., Deng, L., Wang, K., & Zhou, B. (2017). Quantitative analysis of geophysical sources of common mode component in CMONOC GPS coordinate time series. *Advances in Space Research*, *60*(12), 2896–2909. https://doi.org/10.1016/j.asr.2017.05.002

Figure 1.

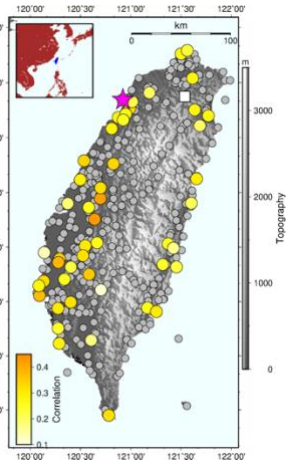
120°00'
120°30'
121°00'
121°30'
122°00'
25°30'
25°00'
24°30'
24°00'
23°30'
23°00'
22°30'
22°00'
km
0
100
m
3000
2000
1000
0
Topography
0.4
0.3
0.2
0.1
Correlation

(a)

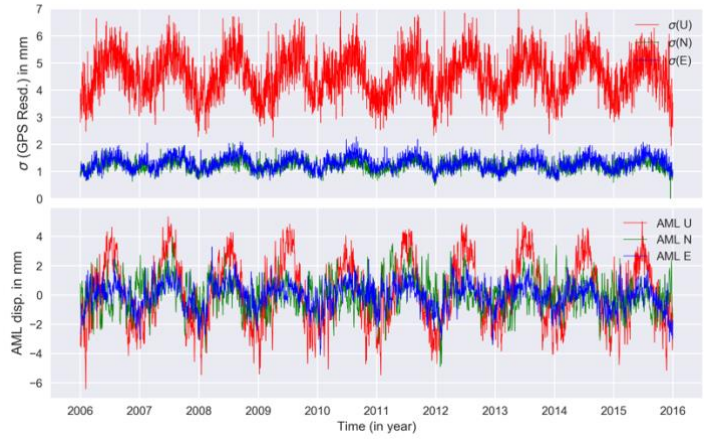
σ (GPS Resd.) in mm
σ(U)
σ(N)
σ(E)
AML disp. in mm
AML U
AML N
AML E
2006
2007
2008
2009
2010
2011
2012
2013
2014
2015
2016
Time (in year)

(b)

Figure 2.

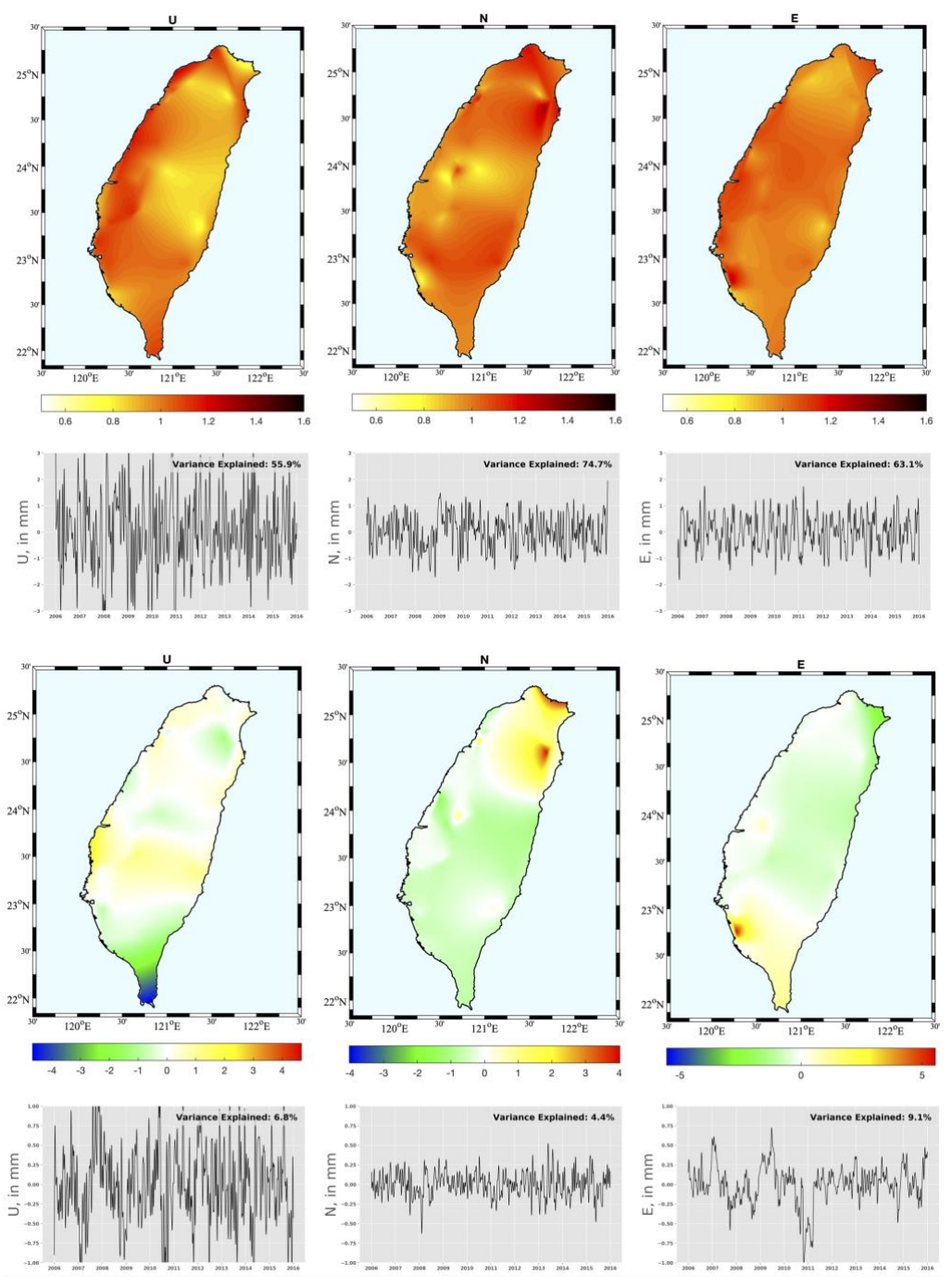
U
N
E
25°N
24°N
23°N
22°N
120°E
121°E
122°E
0.6
0.8
1
1.2
1.4
1.6
Variance Explained: 55.9%
Variance Explained: 74.7%
Variance Explained: 63.1%
U, in mm
N, in mm
E, in mm
2006
2007
2008
2009
2010
2011
2012
2013
2014
2015
2016
-4
-3
-2
-1
0
1
2
3
4
-5
5
Variance Explained: 6.8%
Variance Explained: 4.4%
Variance Explained: 9.1%

Figure 3.

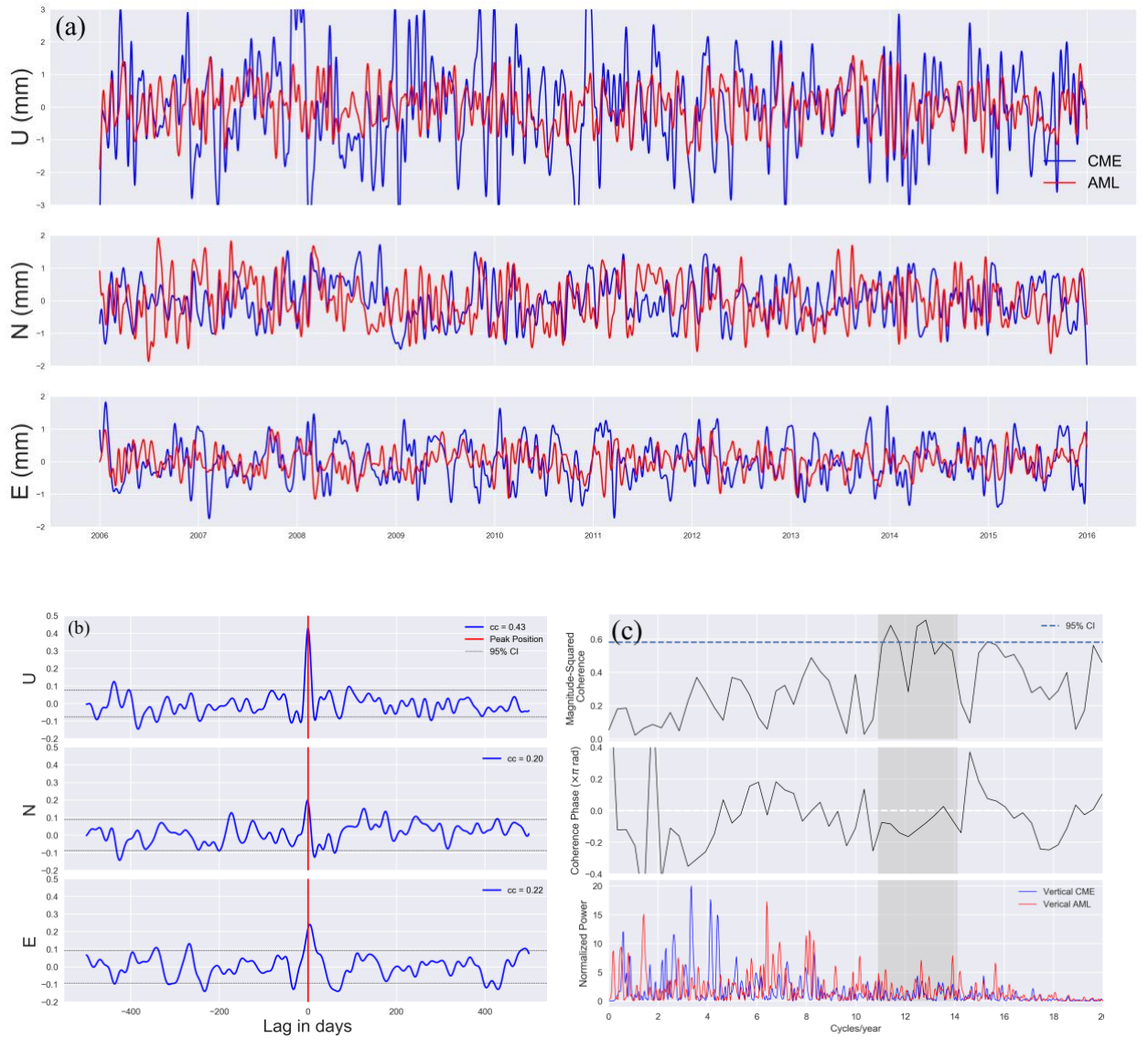
(a)
U (mm)
N (mm)
E (mm)
CME
AML
2006
2007
2008
2009
2010
2011
2012
2013
2014
2015
2016
(b)
cc = 0.43
Peak Position
95% CI
cc = 0.20
cc = 0.22
Lag in days
(c)
95% CI
Magnitude-Squared Coherence
Coherence Phase (×π rad)
Normalized Power
Vertical CME
Verical AML
Cycles/year